AIAA JOURNAL
Vol. 41, No. 10, October 2003

Reynolds-Stress Model Dual-Time-Stepping Computation of Unsteady Three-Dimensional Flows

J. C. Chassaing,* G. A. Gerolymos,† and I. Vallet‡
Université Pierre-et-Marie-Curie, 91405 Paris, France

An efficient and robust implicit methodology for the integration of the unsteady three-dimensional compressible Favre–Reynolds-averaged Navier–Stokes equations with near-wall Reynolds-stress closure is developed. The five mean-flow and seven turbulence transport equations are discretized on a structured deforming grid, using an $\mathcal{O}(\Delta x^3)$ finite volume upwind-biased MUSCL scheme. Time integration uses an implicit $\mathcal{O}(\Delta t^2)$ dual-time-stepping procedure with alternating-direction-implict subiterations (with approximate Jacobians designed to minimize the computing time requirements of the implicit phase for the Reynolds stresses, so that the computational overhead of the Reynolds-stress seven-equation closure, compared to a two-equation closure, is less than 30% per iteration), based on a dynamic criterion of subiterative convergence. Grid-deformation velocities associated with solid-wall displacement are computed using a Laplacian operator. The method is validated by comparison with experimental data for 1) two-dimensional pitching oscillations of a NACA-0012 airfoil and 2) three-dimensional shock-wave oscillation in a transonic channel. The influence of the various parameters of the method is analyzed in detail.

Nomenclature

a	=	sound velocity
$CFL_{\max}$	=	maximum value of the ratio of the physical time step on the stability time step
CFL^*	=	Courant–Fredrichs–Lewy number used for the pseudo time steps [Eq. (17)]
$C_{M1/4}$	=	moment coefficient around the $\frac{1}{4}\chi$ point [Eq. (24)]
C_N	=	normal force coefficient [normal to the airfoil chord; Eq. (24)]
$C_p (C_{p_l}, C_{p_u})$	=	pressure coefficient [on the lower or upper airfoil surface; Eq. (24)]
$\mathcal{D}_{ijk}$	=	diffusion of $\widetilde{u_i'' u_j''}$ (triple correlations, pressure diffusion, and viscous diffusion)
$\mathcal{D}_{\varepsilon_\ell}$	=	diffusion of the turbulence kinetic energy dissipation rate ε
$\mathbb{E}^3$	=	three-dimensional Euclidean space
e_{MF}	=	mean-flow error [Eq. (18)]
$\Im$	=	imaginary part
$\boldsymbol{F}_\ell$	=	ℓ-wise flux [$\in \mathbb{R}^{12}$; Eqs. (3)]
$\boldsymbol{F}_\ell^C$	=	ℓ-wise convective flux [$\in \mathbb{R}^{12}$; Eqs. (3)]
$\boldsymbol{F}^J$	=	approximate flux used for the approximate Jacobians
$\boldsymbol{F}_\ell^V$	=	ℓ-wise diffusive (viscous) flux [$\in \mathbb{R}^{12}$; Eqs. (3)]
$\boldsymbol{F}^\pm$	=	flux-split numerical convective fluxes [Eqs. (2)]
${}^\xi\boldsymbol{F}^N, {}^\eta\boldsymbol{F}^N, {}^\zeta\boldsymbol{F}^N$	=	numerical fluxes for the cell surfaces transverse to the (ξ, η, ζ) grid directions
f	=	frequency
h	=	enthalpy
$\breve{h}_t$	=	total enthalpy of the mean flow $(\tilde{h} + \frac{1}{2}\tilde{u}_i\tilde{u}_i)$ [Eqs. (2) and (3)]
$\widetilde{h'' u_\ell''}$	=	ℓ-wise turbulent heat flux [Eqs. (3)]
(i, j, k)	=	grid indices
K	=	reduced frequency
k	=	turbulence kinetic energy $(\frac{1}{2}\widetilde{u_i'' u_i''})$
ℓ_g	=	grid-cell size used for defining stability time step [Eq. (17)]
ℓ_T	=	turbulence length scale
M (M_{is})	=	Mach number [isentropic Mach number; Eq. (22)]
M_{it}	=	number of subiterations for the solution of the nonlinear system [Eq. (14)]
N_{PP}	=	number of points (instants) per period defining the physical time step [Eq. (16)]
n_ℓ	=	components of the outgoing normal of the control volume $\mathcal{V}_{i,j,k}$ [Eqs. (10)]
p	=	pressure
q_i	=	molecular heat fluxes
$\Re$	=	real part
Re	=	Reynolds number
R_g	=	gas constant $(p = \rho R_g T)$
$\mathbb{R}^{12}$	=	real vector space of dimension 12
r_{MF}	=	mean-flow error reduction monitoring subiterative convergence [Eq. (19)]
$\boldsymbol{S}$	=	vector of source terms [$\in \mathbb{R}^{12}$; Eq. (4)]
$S_{\breve{h}_t}$	=	source term in the mean-flow energy equation[35]
${}^\xi\mathcal{S}_{i\pm1/2,j,k}$, ${}^\eta\mathcal{S}_{i,j\pm1/2,k}$, ${}^\zeta\mathcal{S}_{i,j,k\pm1/2}$	=	cell-face areas of the staggered grid cell $\mathcal{V}_{i,j,k}$
$S_{u_i u_j}$, S_ε	=	source terms for the Reynolds stresses and dissipation rate[35]
Sr	=	Strouhal number

Received 28 August 2002; revision received 31 March 2003; accepted for publication 18 April 2003.

*Research Engineer, Laboratoire d'Energétique, Unité Mixte de Recherche du Centre National de Recherche Scientifique, Building 511, Orsay.

†Professor, Director, Laboratoire d'Energétique, Building 511, Orsay; geg@ccr.jussieu.fr.

‡Assistant Professor, Laboratoire d'Energétique, Unité Mixte de Recherche du Centre National de Recherche Scientifique, Building 511, Orsay.

T = temperature
T_u = turbulence intensity
t = time
U_ℓ = Cartesian components of the grid-displacement velocity
V = velocity
$\mathcal{V}_{i,j,k}$ = control volume of the staggered grid around the point (i, j, k)[42]
VNN^* = von Neumann number used for the pseudo-time steps [Eq. (17)]
$u_i(u, v, w)$ = velocity components
$\boldsymbol{w}$ = vector of conservative variables in the Cartesian frame of reference [Eq. (2)]
$x_\ell(x, y, z)$ = Cartesian system of coordinates
α = angle of attack
γ = isentropic exponent
Δt = time step
$\delta \mathrm{CPU}_{m_{\mathrm{it}}}$ = computing time required for one subiteration
δ_{ij} = Kronecker symbol (components of the order-2 identity tensor)
$\partial\mathcal{V}_{i,j,k}$ = surface bounding $\mathcal{V}_{i,j,k}$
ε^* = turbulence kinetic energy modified dissipation rate[62]
ν = kinematic viscosity
ρ = density
τ_{ij} = viscous stresses
φ = phase angle
χ = airfoil chord

Subscripts

i, j, k, ℓ = vector or tensor components along the corresponding direction or coordinate
l, u = lower and upper airfoil surfaces
MF = mean flow (Favre–Reynolds-averaged quantities)
RSM = turbulence quantities (Reynolds stresses and dissipation rate)
T = turbulent
t = total thermodynamic quantities
w = wall
x, y, z = vector or tensor components along the corresponding coordinate
ξ, η, ζ = coordinates along grid lines (i, j, k, respectively)
χ = based on profile chord χ
∞ = conditions at infinity

Superscripts

m = subiteration counter in the dual-time-stepping procedure [Eq. (14)]
n = time level of the numerical discretization
T = transpose
$\tilde{}$ = Favre average
$''$ = Favre fluctuations
$\bar{}$ = Reynolds average (ensemble average)
$\breve{}$ = function of averaged quantities that is neither a Favre average nor a Reynolds average[35]

Introduction

FAVRE–REYNOLDS-AVERAGED Navier–Stokes solvers are being increasingly used for the prediction of unsteady flows over complex configurations caused by solid boundary displacement[1–5] or vibration,[6–9] induced by applied external perturbations either prescribed[10,11] or dynamically adapted for active control,[12] or associated with low-frequency large-scale system instabilities,[13–17] eventually coupled with structural oscillations.[18–20] In all of these cases, it is tacitly assumed that the characteristic frequencies of the phenomenon are sufficiently low, compared to the characteristic frequencies of turbulence,[21,22] so that statistical closures can be used without any particular correction between resolved and nonresolved scales.[23]

Most of these methods still use simple zero-equation[1,6,15–18,20] or one-equation[3,12,19] turbulence closures. An increasing number of investigators use two-equation closures,[2,4,5,10,11,13,14,24–27] which have the advantage of avoiding the ambiguity that comes from the difficulty of defining length scales, necessary in zero-equation and one-equation closures.[25] Most of the three-dimensional unsteady applications using multiequation turbulence models concern turbomachinery flows with rotor/stator interaction. The basic reason for this is that, in contrast to external aerodynamic applications where often the thin shear-layer approximation is used,[6,7] the flows of interest in turbomachinery 1) are dominated by viscous effects (tip-clearance vortex and secondary flows); 2) often contain large regions of separated flow, especially in compressors, where large separation can be present at the nominal operating point; and 3) the wake development must be described with sufficient accuracy to predict correctly the interaction of the wake with the downstream blade row.

The use of full Reynolds-stress model (RSM) seven-equation closures is obviously the next step.[28] The decisive advantage of taking into account the anisotropy, without the restrictive assumptions of algebraic Reynolds-stress models[29] or explicit algebraic Reynolds-stress models,[30] is currently being exploited by an increasing number of investigators who use near-wall RSMs for steady flows.[31–36] The same improvements are expected for unsteady flows of the type investigated here because the predictive quality of the underlying steady flow is essential for the satisfactory prediction of the unsteady flow around the average value. Substantial modeling work is still necessary, including better modeling of the redistribution terms,[37,38] improved description of the turbulence-dissipation tensor,[39] correct modeling of the compressibility effects,[40] or full RSM multiscale closures.[41] This work cannot, however, be performed, unless efficient and robust RSM Navier–Stokes solvers are available for model evaluation in complex three-dimensional flows around realistic configurations.[42]

There are very few (only three to the authors' knowledge) three-dimensional solvers using seven-equation near-wall RSM closures[42,43–45] that do not use wall functions and that have been successfully applied to three-dimensional transonic flows, with shock-wave/boundary-layer interaction and large separation.[32–36,38] To the authors' knowledge the present work is the first attempt to implement near-wall RSM closures for unsteady flow computations.

The application of the dual-time-stepping (DTS) technique[46–49] has rendered possible the unsteady computation of several complex configurations, where very large differences exist between the maximum and minimum cell sizes, a typical example being the computation of unsteady flow through turbomachinery tip clearance[4] using fine grids. This is because implicit non-DTS methods have a maximum physical time-step limitation (because of the approximations introduced in the implicit phase and in the implicit application of the boundary conditions) that is greatly increased when using DTS techniques, as was demonstrated by Rumsey et al.[48] [who used an implicit upwind scheme with an approximately factored/alternating-direction-implicit (AF-ADI) solver for the linear systems] and Dubuc et al.[49] (who used an implicit upwind scheme with a preconditionned conjugate-gradient solver for the linear systems). Both of these groups of researchers[48,49] showed that the maximum time step could be increased by at least an order of magnitude when using DTS. The DTS technique, where, at each physical time step, a subiterative pseudo-time technique is used to solve the nonlinear system of discretized equations, allows 1) the improvement of the efficiency of the scheme by using non-time-consistent techniques

for the subiterations[47] and 2) the ensuring of $\mathcal{O}(\Delta t^2)$ accuracy, which was rarely achieved by implicit schemes that did not include subiterations.[49] Of course, the use of the DTS technique introduces the choice of the physical time step (time-discretization grid) and the level of convergence of the subiterations, as additional important numerical parameters. Rumsey et al.[48] and Dubuc et al.[49] have conducted detailed studies on the influence of these two parameters on the precision of the numerical method. Recently, Chassaing et al.[42] have used the DTS technique for steady flows, using local time steps both for the time advancement and for the pseudo-time subiterations (LDTS) and obtained substantial improvements in computational efficiency for flows with large separation, using RSM closures.

The purpose of the present paper is to develop an efficient and robust method for the computation of compressible unsteady flows, using the three-dimensional Navier–Stokes equations with near-wall wall-normal-free RSM closure. It is based on the extension of an analogous steady flow method[42] to unsteady flows on dynamic grids. The method uses an implicit upwind-biased discretization with dual time stepping. The computational efficiency of the method is substantially improved by an appropriate approximation of the implicit matrices, which minimizes the computational cost of the turbulence transport equations. An initial two-dimensional validation of the method and parametric studies of the numerical parameters are presented for pitching oscillations of a NASA-0012 profile.[50] Then the method is validated through comparison with measurements for three-dimensional shock-wave oscillation in a transonic nozzle, caused by fluctuating backpressure.[51]

Flow Model and Computational Method

Flow Model

The flow is modeled by the compressible Favre–Reynolds-averaged three-dimensional Navier–Stokes equations,[35] coupled to the six transport equations for the Reynolds stresses and the transport equation for the turbulence kinetic energy modified dissipation rate,[35] written symbolically (see the detailed description given in published papers[35,42]):

$$\frac{\partial \boldsymbol{w}}{\partial t}+\frac{\partial \boldsymbol{F}_\ell}{\partial x_\ell}+\boldsymbol{S}\equiv\frac{\partial \boldsymbol{w}}{\partial t}+\frac{\partial \boldsymbol{F}_x}{\partial x}+\frac{\partial \boldsymbol{F}_y}{\partial y}+\frac{\partial \boldsymbol{F}_z}{\partial z}+\boldsymbol{S}=0 \tag{1}$$

$$\boldsymbol{w}=\Big[\bar\rho,\ \bar\rho\tilde u,\ \bar\rho\tilde v,\ \bar\rho\tilde w,\ \bar\rho\check h_t-\bar p,\ \bar\rho\widetilde{u''u''},$$

$$\bar\rho\widetilde{u''v''},\ \bar\rho\widetilde{v''v''},\ \bar\rho\widetilde{v''w''},\ \bar\rho\widetilde{w''w''},\ \bar\rho\widetilde{w''u''},\ \bar\rho\varepsilon^*\Big]^T\in\mathbb{R}^{12}$$

$$\boldsymbol{F}_\ell=\boldsymbol{F}_\ell^C+\boldsymbol{F}_\ell^V \tag{2}$$

$$\boldsymbol{F}_\ell^C=\Big[\bar\rho\tilde u_\ell,\ \bar\rho\tilde u_\ell\tilde u+\bar p\delta_{x\ell},\ \bar\rho\tilde u_\ell\tilde v+\bar p\delta_{y\ell},\ \bar\rho\tilde u_\ell\tilde w+\bar p\delta_{z\ell},$$

$$\bar\rho\tilde u_\ell\check h_t,\ \bar\rho\tilde u_\ell\widetilde{u''u''},\ \bar\rho\tilde u_\ell\widetilde{u''v''},\ \bar\rho\tilde u_\ell\widetilde{v''v''},\ \bar\rho\tilde u_\ell\widetilde{v''w''},$$

$$\bar\rho\tilde u_\ell\widetilde{w''w''},\ \bar\rho\tilde u_\ell\widetilde{w''u''},\ \bar\rho\tilde u_\ell\varepsilon^*\Big]^T$$

$$\boldsymbol{F}_\ell^V=\Big[0,\ \bar\rho\widetilde{u_\ell''u''}-\bar\tau_{\ell x},\ \bar\rho\widetilde{u_\ell''v''}-\bar\tau_{\ell y},\ \bar\rho\widetilde{u_\ell''w''}$$

$$-\bar\tau_{\ell z},\ \tilde u_i(\bar\rho\widetilde{u_i''u_\ell''}-\bar\tau_{i\ell})+(\bar q_\ell+\bar\rho\widetilde{h''u_\ell''}),$$

$$-\mathcal{D}_{xx\ell},\ -\mathcal{D}_{xy\ell},\ -\mathcal{D}_{yy\ell},\ -\mathcal{D}_{yz\ell},\ -\mathcal{D}_{zz\ell},\ -\mathcal{D}_{zx\ell},\ -\mathcal{D}_{\varepsilon_\ell}\Big]^T \tag{3}$$

$$\boldsymbol{S}=-\Big[0,0,0,0,S_{\check h_t},S_{uu},S_{uv},S_{vv},S_{vw},S_{ww},S_{wu},S_\varepsilon\Big]^T \tag{4}$$

The terms $\mathcal{D}_{ijk}$, $\mathcal{D}_{\varepsilon_\ell}$, $S_{\check h_t}$, S_ε, $S_{u_iu_j}$, and $\widetilde{h''u_\ell''}$ depend on the particular closure used. In the computational examples reported in the present paper, two RSM models were used [the Gerolymos–Vallet model[35] (GV) and a wall-normal-free version[38] of the Launder–Shima model[52] (GSV-LSS)], but the numerical implementation described in the following can be used with other closures.

Space Discretization

These equations [Eqs. (1)] are discretized on a structured dynamically deforming grid, using a finite volume technique, with vertex storage[53–55]:

$$\frac{\mathrm{d}}{\mathrm{d}t}\left[\iiint_{\mathcal{V}_{i,j,k}}\boldsymbol{w}\,\mathrm{d}\mathcal{V}\right]+\iint_{\partial\mathcal{V}_{i,j,k}}(\boldsymbol{F}_\ell-\boldsymbol{w}U_\ell)n_\ell\,\mathrm{d}\mathcal{S}$$

$$+\iiint_{\mathcal{V}_{i,j,k}}\boldsymbol{S}\,\mathrm{d}\mathcal{V}=0 \tag{5}$$

where $\mathcal{V}_{i,j,k}$ is bounded by the cell surface $\partial\mathcal{V}_{i,j,k}$, with outgoing-normal components n_ℓ. The divergence of convective fluxes augmented by the grid-displacement effect ($[\boldsymbol{F}_x^C-\boldsymbol{w}U_x,\ \boldsymbol{F}_y^C-\boldsymbol{w}U_y,\boldsymbol{F}_z^C-\boldsymbol{w}U_z]^T\in\mathbb{R}^{12}\otimes\mathbb{E}^3$) is discretized using the flux-vector-splitting method of Van Leer, as modified by Anderson et al.[56] to take into account the grid-displacement velocities, with $\mathcal{O}(\Delta x^3)$ upwind-biased MUSCL interpolation with limiters (the particular implementation of Anderson et al.[57] was used). The present implementation of the convective fluxes follows closely the work of Anderson et al.[57] and Thomas et al.[58] The divergence of viscous fluxes ($[\boldsymbol{F}_x^V,\boldsymbol{F}_y^V,\boldsymbol{F}_z^V]^T\in\mathbb{R}^{12}\otimes\mathbb{E}^3$) is discretized using an $\mathcal{O}(\Delta x^2)$-centered scheme.[42] Defining a staggered grid[42] and noting (ξ,η,ζ) the grid directions (i,j,k), $({}^\xi\mathcal{S}_{i\pm1/2,j,k},\ {}^\eta\mathcal{S}_{i,j\pm1/2,k},\ {}^\zeta\mathcal{S}_{i,j,k\pm1/2})$ the cell-face areas of the staggered grid cell around the point (i,j,k), and $([{}^\xi n_x,{}^\xi n_y,{}^\xi n_z]^T_{i\pm1/2,j,k}$, $[{}^\eta n_x,{}^\eta n_y,{}^\eta n_z]^T_{i,j\pm1/2,k}$, $[{}^\zeta n_x,{}^\zeta n_y,{}^\zeta n_z]^T_{i,j,k\pm1/2})$ the corresponding unit normals (positive in the positive grid direction), the semi discrete scheme can be written

$$\frac{\mathrm{d}\boldsymbol{w}_{i,j,k}}{\mathrm{d}t}+\frac{1}{\mathcal{V}_{i,j,k}}\begin{bmatrix}+{}^\xi\mathcal{S}_{i+\frac12,j,k}\,{}^\xi\boldsymbol{F}^N_{i+\frac12,j,k}-{}^\xi\mathcal{S}_{i-\frac12,j,k}\,{}^\xi\boldsymbol{F}^N_{i-\frac12,j,k}\\ +{}^\eta\mathcal{S}_{i,j+\frac12,k}\,{}^\eta\boldsymbol{F}^N_{i,j+\frac12,k}-{}^\eta\mathcal{S}_{i,j-\frac12,k}\,{}^\eta\boldsymbol{F}^N_{i,j-\frac12,k}\\ +{}^\zeta\mathcal{S}_{i,j,k+\frac12}\,{}^\zeta\boldsymbol{F}^N_{i,j,k+\frac12}-{}^\zeta\mathcal{S}_{i,j,k-\frac12}\,{}^\zeta\boldsymbol{F}^N_{i,j,k-\frac12}\end{bmatrix}$$

$$+\frac{\boldsymbol{w}_{i,j,k}}{\mathcal{V}_{i,j,k}}\frac{\mathrm{d}\mathcal{V}_{i,j,k}}{\mathrm{d}t}+\boldsymbol{S}_{i,j,k}\cong0 \tag{6}$$

In this discretization the cell-volume variation is treated in a semiconservative manner. Although more accurate fully conservative techniques are available,[53–55] the present choice avoids storing the computational grid at various instants and gives satisfactory results for aeroelastic applications. The numerical flux is given by

$${}^\xi\boldsymbol{F}^N_{i\pm\frac12,j,k}=\Big[\boldsymbol{F}^+\big(\boldsymbol{w}^-;{}^\xi n_x,{}^\xi n_y,{}^\xi n_z;U_x,U_y,U_z\big)$$

$$+\boldsymbol{F}^-\big(\boldsymbol{w}^+;{}^\xi n_x,{}^\xi n_y,{}^\xi n_z;U_x,U_y,U_z\big)+\boldsymbol{F}_\ell^V{}^\xi n_\ell\Big]_{i\pm\frac12,j,k} \tag{7}$$

The Van Leer fluxes $\boldsymbol{F}^\pm(\boldsymbol{w};n_x,n_y,n_z;U_x,U_y,U_z)$ are given by

$$\boldsymbol{F}^{\pm} = \underbrace{\begin{bmatrix} 0 \\ 0 \\ 0 \\ 0 \\ 0 \\ 0 \\ 0 \\ 0 \\ 0 \\ 0 \\ 0 \\ 0 \end{bmatrix}}_{\pm\breve{M}_n < -1}, \qquad \underbrace{\pm\bar{\rho}\breve{a}\frac{(\breve{M}_n \pm 1)^2}{4}\begin{bmatrix} 1 \\ n_x\frac{\breve{a}}{\gamma}(-\breve{M}_n \pm 2) + \tilde{u} \\ n_y\frac{\breve{a}}{\gamma}(-\breve{M}_n \pm 2) + \tilde{v} \\ n_z\frac{\breve{a}}{\gamma}(-\breve{M}_n \pm 2) + \tilde{w} \\ \frac{-(\gamma-1)\breve{M}_n^2 \pm 2(\gamma-1)\breve{M}_n + 2}{\gamma^2-1}\breve{a}^2 + \frac{\tilde{V}^2}{2} + \frac{U_n}{\gamma}(-\tilde{V}_n \pm 2\breve{a}) \\ \widetilde{u''u''} \\ \widetilde{u''v''} \\ \widetilde{v''v''} \\ \widetilde{v''w''} \\ \widetilde{w''w''} \\ \widetilde{w''u''} \\ \varepsilon^* \end{bmatrix}}_{|\breve{M}_n| \le 1}, \qquad \underbrace{\begin{bmatrix} \bar{\rho}\tilde{V}_n \\ \bar{\rho}\tilde{V}_n\tilde{u} + \bar{p}n_x \\ \bar{\rho}\tilde{V}_n\tilde{v} + \bar{p}n_y \\ \bar{\rho}\tilde{V}_n\tilde{w} + \bar{p}n_z \\ \bar{\rho}\tilde{V}_n\tilde{h}_t + \bar{p}U_n \\ \bar{\rho}\tilde{V}_n\widetilde{u''u''} \\ \bar{\rho}\tilde{V}_n\widetilde{u''v''} \\ \bar{\rho}\tilde{V}_n\widetilde{v''v''} \\ \bar{\rho}\tilde{V}_n\widetilde{v''w''} \\ \bar{\rho}\tilde{V}_n\widetilde{w''w''} \\ \bar{\rho}\tilde{V}_n\widetilde{w''u''} \\ \bar{\rho}\tilde{V}_n\varepsilon^* \end{bmatrix}}_{\pm\breve{M}_n > 1} \tag{8}$$

where $\breve{M}_n(\boldsymbol{w}; n_x, n_y, n_z; U_x, U_y, U_z) = [\tilde{u}_\ell(\boldsymbol{w}) - U_\ell]n_\ell\breve{a}^{-1}(\boldsymbol{w}) = \tilde{V}_n\breve{a}^{-1}$ is the normal Mach number relative to the moving grid and $\breve{a}(\boldsymbol{w}) = \sqrt{[\gamma R_g \tilde{T}(\boldsymbol{w})]}$ is the sound velocity. The MUSCL variables are defined by an $\mathcal{O}(\Delta x^3)$ upwind-biased interpolation, identical to the one used for the steady version of the method.[42]

Grid Displacement

The grid velocities necessary for the definition of the numerical fluxes are computed by solving a Laplace equation

$$\nabla^2 U_x = \nabla^2 U_y = \nabla^2 U_z = 0 \tag{9}$$

with Dirichlet boundary conditions prescribing the solid-wall displacement velocities.[59] These velocities are also used to compute the cell-volume variation term [Eq. (4)] using the identity[53–55]

$$\frac{\mathrm{d}\mathcal{V}_{i,j,k}}{\mathrm{d}t} \equiv \frac{\mathrm{d}}{\mathrm{d}t}\left[\int\int\int_{\mathcal{V}_{i,j,k}} \mathrm{d}\mathcal{V}\right] = \int\int_{\partial\mathcal{V}_{i,j,k}} U_\ell n_\ell \,\mathrm{d}\mathcal{S}$$

$$= \begin{bmatrix} +{}^{\xi}\mathcal{S}_{i+\frac{1}{2},j,k}\,{}^{\xi}U_{i+\frac{1}{2},j,k} - {}^{\xi}\mathcal{S}_{i-\frac{1}{2},j,k}\,{}^{\xi}U_{i-\frac{1}{2},j,k} \\ +{}^{\eta}\mathcal{S}_{i,j+\frac{1}{2},k}\,{}^{\eta}U_{i,j+\frac{1}{2},k} - {}^{\eta}\mathcal{S}_{i,j-\frac{1}{2},k}\,{}^{\eta}U_{i,j-\frac{1}{2},k} \\ +{}^{\zeta}\mathcal{S}_{i,j,k+\frac{1}{2}}\,{}^{\zeta}U_{i,j,k+\frac{1}{2}} - {}^{\zeta}\mathcal{S}_{i,j,k-\frac{1}{2}}\,{}^{\zeta}U_{i,j,k-\frac{1}{2}} \end{bmatrix} \tag{10}$$

where ${}^{\xi}U_{i\pm1/2,j,k} = {}^{\xi}[U_\ell n_\ell]_{i\pm1/2,j,k}$ is the projection of the grid-displacement velocity on the unit normal of the cell face.

Implicit Dual Time Stepping

Denoting by $\boldsymbol{\mathcal{L}}_{i,j,k}$ the discretized form of the space operator [divergence, volume variation, and source terms; Eq. (3)], the semidiscrete equation at grid point (i, j, k) gives

$$\frac{\mathrm{d}\boldsymbol{w}_{i,j,k}}{\mathrm{d}t} + \boldsymbol{\mathcal{L}}_{i,j,k} \cong 0 \quad \forall i, j, k \iff \frac{\mathrm{d}\mathfrak{w}}{\mathrm{d}t} + \mathfrak{L}(\mathfrak{w}) \cong 0 \tag{11}$$

where $\mathfrak{w} = [\boldsymbol{w}_{1,1,1}, \boldsymbol{w}_{1,1,2}, \ldots, \boldsymbol{w}_{N_i,N_j,N_k}]^T \in \mathbb{R}^{12\times N_i\times N_j\times N_k}$ and $\mathfrak{L} = [\boldsymbol{\mathcal{L}}_{1,1,1}, \boldsymbol{\mathcal{L}}_{1,1,2}, \ldots, \boldsymbol{\mathcal{L}}_{N_i,N_j,N_k}]^T \in \mathbb{R}^{12\times N_i\times N_j\times N_k}$, are the global vectors of the unknowns and of the space operators, respectively. The time discretization of the semidiscrete scheme uses a $\mathcal{O}(\Delta t^2)$ implicit scheme. The resulting system of nonlinear equations is solved using a dual-time-stepping iterative technique.[46–49] Denoting Δt as the physical time step and $\Delta t^*_{i,j,k}$ the local dual-pseudo-time step at grid point (i, j, k) and defining the diagonal matrix

$$\Delta\mathfrak{t}^* = \mathrm{diag}\left[\left(\Delta t^*_{1,1,1}\right)\underline{I}_{12}, \left(\Delta t^*_{1,1,2}\right)\underline{I}_{12}, \ldots, \left(\Delta t^*_{N_i,N_j,N_k}\right)\underline{I}_{12}\right] \tag{12}$$

where $\underline{I}_{12}$ denotes the 12×12 identity matrix, the numerical scheme between instants n and $n+1$, for the dual subiteration m, can be written

$$\frac{3[{}^{n+1}\mathfrak{w}] - 4[{}^{n}\mathfrak{w}] + [{}^{n-1}\mathfrak{w}]}{2\Delta t} + \mathfrak{L}({}^{n+1}\mathfrak{w}) \cong 0$$

$$\Longrightarrow \frac{{}^{m+1,n+1}\mathfrak{w} - {}^{m,n+1}\mathfrak{w}}{\Delta\mathfrak{t}^*} + \frac{3[{}^{m+1,n+1}\mathfrak{w}] - 4[{}^{n}\mathfrak{w}] + [{}^{n-1}\mathfrak{w}]}{2\Delta t}$$

$$+ \mathfrak{L}({}^{m,n+1}\mathfrak{w}) + \frac{\partial\mathfrak{L}^J}{\partial\mathfrak{w}}({}^{m,n+1}\mathfrak{w})[{}^{m+1,n+1}\mathfrak{w} - {}^{m,n+1}\mathfrak{w}] \cong 0 \tag{13}$$

where $\mathfrak{L}^J(\mathfrak{w})$ is an approximation to the operator $\mathfrak{L}(\mathfrak{w})$, chosen so as to minimize implicit work.[42] (The baseline choice $\mathfrak{L}^J = \mathfrak{L}$ uses the exact Jacobian in the implicit procedure.) The following iterative procedure is obtained: Do $m_{\mathrm{it}} = 1, M_{\mathrm{it}}$ (subiterations)

$$\left[\mathfrak{I} + \Delta\mathfrak{t}^{**}\frac{\partial\mathfrak{L}^J}{\partial\mathfrak{w}}({}^{m,n+1}\mathfrak{w})\right][{}^{m+1,n+1}\mathfrak{w} - {}^{m,n+1}\mathfrak{w}]$$

$$\cong -\Delta\mathfrak{t}^{**}\left[\frac{3[{}^{m,n+1}\mathfrak{w}] - 4[{}^{n}\mathfrak{w}] + [{}^{n-1}\mathfrak{w}]}{2\Delta t} + \mathfrak{L}({}^{m,n+1}\mathfrak{w})\right] \tag{14}$$

where $\mathfrak{I} \in \mathbb{R}^{(12\times N_i\times N_j\times N_k)\times(12\times N_i\times N_j\times N_k)}$ is the identity matrix, ${}^{1,n+1}\mathfrak{w} = {}^{n}\mathfrak{w}$, and

$$\Delta\mathfrak{t}^{**} = \frac{\Delta\mathfrak{t}^*}{\mathfrak{I} + (3/2\Delta t)\Delta\mathfrak{t}^*} \equiv \left[\mathfrak{I} + \frac{3}{2\Delta t}\Delta\mathfrak{t}^*\right]^{-1}\Delta\mathfrak{t}^* \tag{15}$$

Note that the usual non-dual-time-stepping scheme[57,56] is recovered at the limit $\Delta\mathfrak{t}^* \longrightarrow \infty \iff \Delta\mathfrak{t}^{**} = \frac{2}{3}\Delta t\mathfrak{I}$, with only one subiteration ($M_{\mathrm{it}} = 1$).

Approximate Jacobians

The computational cost of the RSM method (and the corresponding overhead in comparison with more conventional two-equation closures) is basically caused a) by the computation and assembly

of the Jacobian $\partial\mathfrak{L}^J/\partial\mathfrak{w}$ and b) by the solution of the linear system [Eq. (14)]. The approximate jacobian is computed by replacing the numerical fluxes $\boldsymbol{F}^N$ [Eqs. (7) and (8)] by approximate fluxes $\boldsymbol{F}^J = \boldsymbol{F}^{CJ} + \boldsymbol{F}^{VJ}$. The following approximations were made[42]:

1) The convective discretization is computed by taking the derivative of an $\mathcal{O}(\Delta x)$ stencil instead of the $\mathcal{O}(\Delta x^3)$ stencil used for the computation of the numerical fluxes, which is equivalent to computing the convective part of the approximate fluxes $\boldsymbol{F}^{CJ}$ with MUSCL variables in $\boldsymbol{F}^{\pm}$ [Eq. (8)] obtained using $\mathcal{O}(\Delta x)$ extrapolation.[57]

2) If no other particular approximation of the Jacobians is made, then the computational overhead of the RSM method in comparison with two-equation closures is easily estimated,[42] to a factor of almost three, a drawback that is raised by an ad hoc diagonalization of the viscous Jacobians, obtained by using approximate viscous fluxes $\boldsymbol{F}^{VJ}$ such that $\partial\boldsymbol{F}^{VJ}_{\ell}/\partial x_{\ell}$ corresponds to an approximate discretization of $\mathrm{div}(\nu_{eq}\,\mathrm{grad}\,w_p)$ for every element w_p of $\boldsymbol{w} = (w_p;\ p = 1, \ldots, 12)$ except $w_1 = \bar{\rho}$ (no diffusive fluxes in the continuity equation), where ν_{eq} is an equivalent diffusivity.[42]

3) Source-term Jacobians were neglected.

The detailed form of $\mathfrak{L}^J$ and the associated Jacobian $\partial\mathfrak{L}^J/\partial\mathfrak{w}$ are given in Chassaing et al.,[42] where it is shown that the introduction of the preceding approximations modifies the ratio of computational effort per subiteration between two-equation and seven-equation closures to 1:1.26 (a very substantial gain indeed compared to the initial 1:4 ratio obtained when the preceding approximations are not used[32]).

Approximate Factorization and Boundary Conditions

In the present work the linear systems appearing at every subiteration [Eq. (14)] are solved using an approximately factored ADI-AF method.[42] The three successive spacewise linear systems are solved using banded-LU factorization.[42] To achieve the high time steps used, it is indispensible to apply boundary conditions both implicitly and explicitly. Boundary conditions are treated using the method of characteristics and are treated implicitly following the corrections method of Chakravarthy,[42,44] applied to each linear system of the ADI-AF.

Time Stepping

The time step Δt is chosen on the basis of the physical phenomenon studied and determines the temporal resolution of the simulation. The flows considered in the present work are time periodic of known frequency f. (They are caused by either an applied time-periodic external perturbation or by time-periodic motion of the solid boundaries.) For such flows the time step is chosen by prescribing the number of instants per period N_{PP} that will be simulated:

$$\Delta t = 1/(f N_{PP}) \tag{16}$$

The dual local pseudo-time step is based on a combined convective (Courant) and viscous (von Neumann) criterion[42]:

$$\Delta t^*_{i,j,k} \le \min\left(CFL^*\left\{\ell_g \Big/ \left[\tilde{V} + \breve{a}\sqrt{1 + \tfrac{5}{6}(\gamma - 1)M_T^2}\right]\right\},\ VNN^*\left[\ell_g^2 \Big/ (2\nu_{eq})\right]\right) \tag{17}$$

where $\tilde{V}$ is the flow velocity, $\breve{a}$ is the sound velocity, $M_T = \sqrt{(2k\breve{a}^{-2})}$ is the turbulence Mach number, and ν_{eq} is the equivalent diffusivity, introduced by MacCormack (see Ref. 42). Typical choices of the stability parameters are $CFL^* = VNN^* = 10 - 20$.

Positivity, Boundedness, and Realizability Constraints

It is quite possible, during the subiterations, to have Reynolds stresses that do not satisfy the realizability constraints introduced by Schumann.[60] Such anomalous behavior is systematically checked for at every subiteration. If the realizability constraints are not satisfied for a given grid point, then all turbulence variables are set to zero at this grid point.[42] These simple realizability and boundedness fixes (which are completely explicit and as a consequence easy to implement) stabilize the computations for all of the cases studied using this method.[32,35,36,42] In subsequent subiterations turbulence builds up again through diffusion from neighboring nodes.

Computational Parameters

The parameters controlling the numerical scheme (time integration) are the number of instants per period N_{PP}, the CFL number CFL^* for the dual pseudo-time step (assuming that $VNN^* = CFL^*$) and the number of subiterations performed at each iteration $M_{it}(n_{it})$. This number is chosen dynamically based on a convergence criterion for the subiterations. The relative variation of the mean flow e_{MF} is monitored using the following error L_2 pseudonorm[42]:

$$e_{MF}[\mathfrak{w}_{MF}, \Delta\mathfrak{w}_{MF}] = \log_{10}\sqrt{\frac{1}{5}\left\{\frac{\sum[\Delta\bar{\rho}]^2}{\sum[\bar{\rho}]^2} + \frac{\sum[\Delta(\bar{\rho}\tilde{u}_i)\Delta(\bar{\rho}\tilde{u}_i)]}{\sum[\bar{\rho}\tilde{u}_i\bar{\rho}\tilde{u}_i]} + \frac{\sum[\Delta(\bar{\rho}\breve{h}_t - \bar{p})]^2}{\sum[\bar{\rho}\breve{h}_t - \bar{p}]^2}\right\}} \tag{18}$$

where $\sum$ implies summation over all of the grid nodes and the summation convention for the Cartesian indices $i,\ j = 1, 2, 3$ is used [meaning for instance that the relative variation of the momentum vector is used in Eq. (18) for e_{MF}]. This quantity is used to define the subiterative convergence of the increment by the error reduction between subiterations $[m, n+1]$ and $[m+1, n+1]$ [Eq. (14)]:

$$r_{MF}(m+1, n+1) = \log_{10}\left\{\frac{10^{[e_{MF}(m+1,n+1)]} - 10^{[e_{MF}(m,n+1)]}}{10^{[e_{MF}(m,n+1)]}}\right\} \tag{19}$$

where $e_{MF}(m+1, n+1) \equiv e_{MF}[{}^n\mathfrak{w}_{MF},\ {}^{m+1,n+1}\mathfrak{w}_{MF} - {}^n\mathfrak{w}_{MF}]$. The reduction r_{MF} indicates approximately the number of digits to which the increment is converged during the subiterations. The time-integration scheme is therefore defined by the triplet $[N_{PP}, CFL^*; M_{it}, r_{MF}] = [N_{PP}, CFL^*; -, r_{MF}]$, where M_{it} is determined dynamically at each time step by the value of r_{MF}. The corresponding quantities for the turbulence variables[42] (e_{RSM} and r_{RSM}) were also monitored, but they were not used in determining $M_{it}(n_{it})$ because r_{RSM} usually diminishes faster than r_{MF}.

Computational Results

Configurations Studied

To validate the computational method for unsteady flows on dynamic grids, comparisons with measurements are presented for a NACA-0012 airfoil, oscillating in pitch around quarter-chord.[50] This is a two-dimensional test case and was used for the systematic evaluation of the parameters of the numerical scheme. This test case is not very sensitive to the turbulence model used, but it was chosen because it is well documented and has been previously used for computational method validation by various authors.[49]

The validity of the method for three-dimensional flows with shock-wave/boundary-layer interaction is further illustrated by considering shock-wave oscillations in a transonic nozzle,[51] caused by fluctuating backpressure, at various frequencies (20, 80, and 180 Hz).

NACA-0012 Airfoil

This is a well-known test case that has been computed by many authors[49] and is known as the AGARD-CT5 test case.[50] The airfoil, whose chord $\chi = 0.1016$ m, was mounted in a wind tunnel with slotted floor and roof walls and oscillated in pitch around quarter-chord. The pitching oscillation was harmonic and resulted in a time variation of the instantaneous angle of attack:

$$\alpha(t) = {}^0\alpha + {}^1\alpha\sin(2\pi f t) \tag{20}$$

where ${}^0\alpha$ is the time-mean angle of attack and ${}^1\alpha$ is the pitching amplitude. The transition is free, both for the experiment and the

Table 1 Computational grids used for the NACA-0012 CT5 test case[50] and steady-flow global normal force and pitching-moment coefficients computed using the Gerolymos–Vallet[35] RSM

Grid	N_i [a,b]	N_j [a,b]	r_j [c]	$r_{i_{LE}}$ [c]	$r_{i_{TE}}$ [c]	n_w^+ [d]	C_N [e]	$C_{M1/4}$ [f]
A	161	61	1.350	1.16	<1.30	<0.35	0.3184×10^{-2}	0.4738×10^{-4}
B	161	91	1.195	1.16	<1.30	<0.40	0.3511×10^{-2}	0.1899×10^{-4}
C	201	91	1.195	1.13	<1.25	<0.40	0.3502×10^{-2}	0.2257×10^{-4}
D	161	131	1.123	1.16	<1.30	<0.35	0.3102×10^{-2}	0.6740×10^{-4}
E	201	111	1.150	1.13	<1.25	<0.40	0.3377×10^{-2}	0.3012×10^{-4}
F	201	211	1.068	1.13	<1.25	<0.40	0.3012×10^{-2}	0.7922×10^{-4}
G	401	211	1.068	1.06	<1.10	<0.40	0.3053×10^{-2}	0.7858×10^{-4}

[a] i, j = grid directions.
[b] N_i, N_j = number of points.
[c] r_j, $r_{i_{LE}}$, $r_{i_{TE}}$ = geometric progression ratio.
[d] n_w^+ = nondimensional distance of the first grid node away from the wall.
[e] C_N = normal force coefficient.
[f] $C_{M1/4}$ = pitching-moment coefficient around $\frac{1}{4}\chi$.

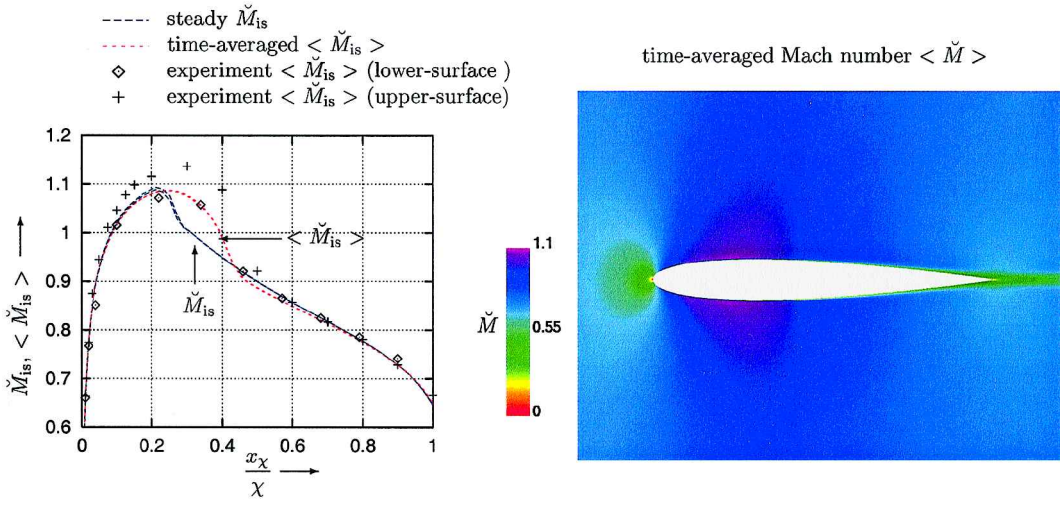

Fig. 1 Comparison of computed isentropic Mach number ($\breve{M}_{is}$ from steady computations using an RSM closure[35] and an LDTS steady time-integration scheme[42] and time-averaged $\langle \breve{M}_{is} \rangle$ from the unsteady computations of Fig. 2) and measured[50] time-averaged $\langle \breve{M}_{is} \rangle$ distributions on the NACA-0012 airfoil surface ($M_\infty = 0.755$, $Re_\chi = 5.5 \times 10^6$, pitching oscillations around $\frac{1}{4}\chi$, $Sr_\chi = 0.0259$; grid G).

computations. The experimental values of the normal force coefficient C_N, the pitching-moment coefficient $C_{M1/4}$, and the angle-of-attack parameters α, ${}^0\alpha$, and ${}^1\alpha$ have been corrected by Landon[50] to take into account the wall interferences related to the small tunnel-height-to-airfoil-chord ratio of 4.5.

The computational grid[59] is an O-grid, geometrically stretched with ratio r_j away from the blade, and adjusted, at the farfield, to a square, whose sides are parallel to the incoming flow.[59] The grid points on the airfoil surface are stretched geometrically,[61] near the leading edge (with ratio $r_{i_{LE}}$) and near the trailing edge (with ratio $r_{i_{TE}}$), and the O-grid is generated biharmonically.[61] The grid is also stretched in the region of the wake, transversally.[59] All of the grids used extended $\sim 17\chi$ away from the airfoil,[48,49] and far-field boundary conditions were applied using the method of Riemann invariants.[19,25] The computations (Fig. 1) were run at the experimental conditions

$$M_\infty = 0.755, \quad Re_\chi = 5.5 \times 10^6, \quad T_{t_\infty} = 280\ \text{K}$$
$$p_{t_\infty} = 382{,}197.9\ \text{Pa}, \quad T_{u_\infty} = 0.005, \quad \ell_{T_\infty} = 0.1\ \text{m}$$
$$f = 62\ \text{Hz}, \quad {}^0\alpha = 0.016\ \text{deg}, \quad {}^1\alpha = 2.51\ \text{deg}$$
$$K_{\frac{1}{2}} = 0.0814, \quad K = 0.1628, \quad Sr_\chi = 0.0259 \quad (21)$$

where M_∞ is the Mach number at the far field, T_{t_∞} is the total temperature at the far field, p_{t_∞} is the total pressure at the far field, $Re_\chi = V_\infty \chi \nu_\infty^{-1}$ is the Reynolds number, V_∞ is the air velocity at the far field, ν_∞ is the kinematic viscosity at the farfield, $K = 2\pi f \chi V_\infty^{-1}$ is the reduced frequency based on chord length, $K_{1/2} = \frac{1}{2}K$ is the reduced frequency based on half-chord length, and $Sr_\chi = f\chi V_\infty^{-1}$ is the Strouhal number. No information on turbulence intensity $T_{u_\infty} = \sqrt{(\frac{2}{3}k_\infty)} V_\infty^{-1}$ or turbulence length scale $\ell_{T_\infty} = k_\infty^{3/2} \varepsilon_\infty^{-1}$ at the far field was available in the experimental database,[50] so that the values used were chosen arbitrarily (k_∞ and ε_∞ are the turbulence kinetic energy and its dissipation rate at the far field). Although these quantities can have a nonnegligible influence on the development of the boundary layers on the airfoil surface, for the particular case considered here the pressure distributions on the airfoil are not substantially influenced by viscous effects. (This is substantiated by the satisfactory agreement with measurements obtained by Dubuc et al.[49] using Euler equations.) For this reason no parametric study on T_{u_∞} and ℓ_{T_∞} was undertaken. A preliminary grid-influence study was conducted for steady flow conditions at the time-mean angle of attack $\alpha_\infty = {}^0\alpha$, concerning both i-wise (around the blade) and j-wise refinement (Table 1). Although some small differences are observed in the force and moment coefficients (both are very near 0 because of the very slight angle of attack and the symmetric geometry of the airfoil), the pressure distributions on the airfoil surface are practically identical between the different grids.

Computed instantaneous pressure distributions on the airfoil (Fig. 2), for various instants in the period, are in excellent agreement with measurements on the lower surface, but underestimate the upper-surface shock strength at the higher positive incidences ($2\ \text{deg} \le \alpha \le 2.5\ \text{deg}$). The pressure distributions are presented in the form of isentropic Mach number

$$\breve{M}_{is}(\bar{p}, p_{t_\infty}) = \sqrt{\left\{[2/(\gamma-1)]\left[(p_{t_\infty}/\bar{p})^{(\gamma-1)/\gamma} - 1\right]\right\}} \quad (22)$$

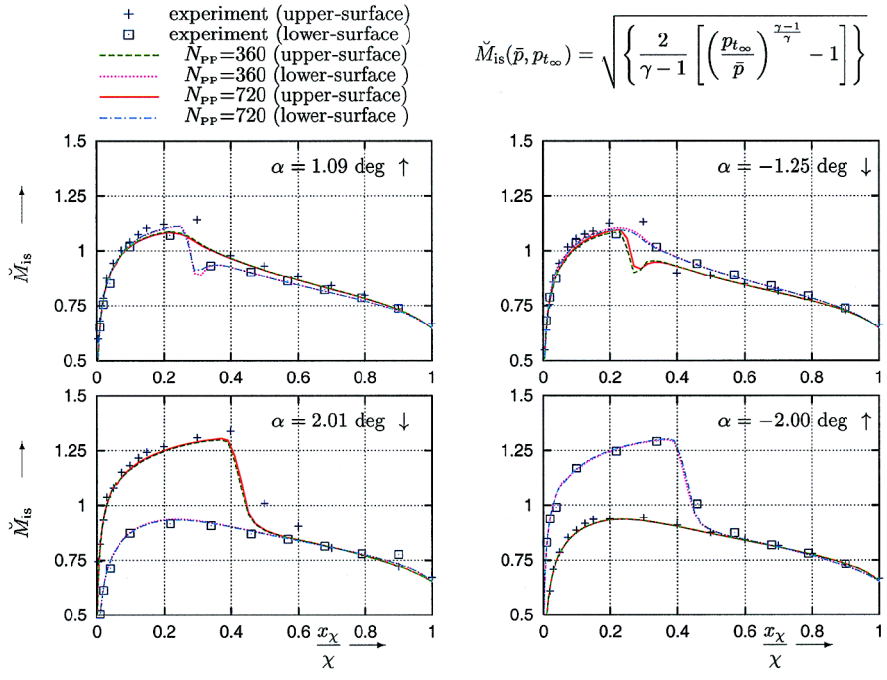

Fig. 2 Comparison of computed (using an RSM closure[35] and the $[N_{PP}, CFL^*; M_{it}, r_{MF}] = [360, 10; -, -1.5]$, $[720, 10; -, -1.5]$ time-integration DTS schemes) and measured[50] instantaneous $\breve{M}_{is}$ distributions for various values of instantaneous angle of attack $\alpha(t)$ [Eq. (20); ↓, nose-down motion of the airfoil; ↑, nose-up motion of the airfoil] on the NACA-0012 airfoil surface ($M_\infty = 0.755, Re_\chi = 5.5 \times 10^6$, pitching oscillations around $\frac{1}{4}\chi$, $Sr_\chi = 0.0259$; grid B).

which is directly related to the pressure coefficient C_p. The discrepancy on the upper surface is better understood by considering the time-mean value of the isentropic Mach number, both measured and computed (Fig. 1):

$$\langle \breve{M}_{is} \rangle = f \int_{t_0}^{t_0 + f^{-1}} \breve{M}_{is}(t)\, dt \tag{23}$$

The agreement is again excellent on the lower surface, as the unsteady effects smear the pressure distribution in the shock-wave neighborhood, in agreement with the time-averaged value of the measurements. However, although the computed results are almost symmetrical between the upper surface and the lower surface there is a noticeable difference in the mesurements. This experimentally observed asymmetry cannot be explained by the negligible mean incidence ${}^0\alpha = 0.016$ deg. The causes of the experimental data asymmetry are not clear (some preliminary tests of M_∞ and α_∞ variation were not conclusive), but this asymmetry should be remembered when comparing unsteady global force and moment coefficients

$$C_N = \int_0^1 (C_{p_l} - C_{p_u})\, d\left(\frac{x_\chi}{\chi}\right)$$

$$C_{M\frac{1}{4}} = \int_0^1 (C_{p_l} - C_{p_u})\left(\frac{1}{4} - \frac{x_\chi}{\chi}\right) d\left(\frac{x_\chi}{\chi}\right), \qquad C_p = \frac{\bar{p} - p_\infty}{\frac{1}{2}\rho_\infty V_\infty^2} \tag{24}$$

Measured C_N and $C_{M1/4}$ were compared (Fig. 3) with computations using the 161×91 grid B (Table 1) for various values of physical time step (number of instants per period $N_{PP} = 90$, 180, 360, 720, 1440) with a reduction $r_{MF} = -1.5$ (Figs. 3c and 3d) and for various values of reduction ($r_{MF} = -1$, -1.5, -2, -2.3) with $N_{PP} = 360$ (Figs. 3a and 3b). Satisfactory agreement (and numerical convergence) is achieved with the scheme [360, 10; −, −1.5], but it is noteworthy that stable computations are obtained for even larger physical time steps, corresponding to $CFL_{max} \sim 2 \times 10^6$ (Table 2). These values of CFL_{max} are quite large indeed and corroborate the general experience of the authors,[32,35,36,42] that well-implemented RSMs are more stable than zero-equation, one-equation, or even two-equation closures. As far as the influence of reduction is concerned, it is observed that $r_{MF} = -1$ is insufficient to obtain numerically converged results for $C_{M1/4}$ (Fig. 3d), although the results obtained for C_N (Fig. 3c) are satisfactory.

Three-Dimensional Transonic Channel

The validity of the method is further illustrated by considering shock-wave oscillations in a transonic nozzle.[51] The experimental setup has been described in detail by Ott et al.[51] On the nozzle liners the boundary layer was cut off before the throat, whereas on the side walls the boundary layers were not modified. (These relatively thick side-wall boundary layers interact with the shock wave at the nozzle corners and produce the significant three-dimensional blockage effects observed.) At the exit section of the nozzle, a rotating cylindrical rod with elliptical cross section induces a shock wave in the test section, which oscillates with the rotation of the rod.[51]

Previous unsteady three-dimensional computations of this configuration[10] for a frequency of 180 Hz, using the Launder–Sharma[62] k–ε model, have shown quite satisfactory agreement with experimental measurements. This previous study[10] used an $\mathcal{O}(\Delta t)$ non-DTS AF-ADI method (approximately factored alternating-directions-implicit), without subiterations. The computations were run with $CFL_{max} = 500$ and required $N_{PP} = 15{,}408$ instants per period. At the time of this previous study,[10] the high required computing times precluded the computations of lower frequency excitations (for which experimental data were available[51]), for which model one- and-one-half Euler computations demonstrated however that the flow was not quasi-steady.[10]

In the present work this configuration was studied using the DTS method, with both the Launder–Sharma[62] k–ε model and a wall-normal-free version of the Launder–Shima[52] model (GSV-LSS), developed by the authors.[38] Only $\frac{1}{4}$ of the nozzle was discretized (Table 3). At the inflow boundary a reservoir condition was applied (because the flow is choked and no significant perturbation reaches the inflow boundary), using the experimentally determined conditions[51]

$$p_{t_i} = 168{,}600\ \text{Pa}, \qquad T_{t_i} = 323\ \text{K}, \qquad \delta_{y_i} = 0.5\ \text{mm}$$
$$\delta_{z_i} = 5\ \text{mm}, \qquad T_{u_i} = 1.6\%, \qquad \ell_{T_i} = 0.3\ \text{mm} \tag{25}$$

where δ_{y_i} is the boundary-layer thickness at inflow on the nozzle liners, δ_{z_i} the boundary-layer thickness at inflow on the side wall, p_{t_i} the inflow total pressure outside the boundary layers, T_{t_i} the inflow total temperature outside the boundary layers, T_{u_i} the turbulence intensity at inflow, and ℓ_{T_i} the turbulence length scale at inflow. The boundary-layer thicknesses at inflow were approximately[10] chosen to represent the thick side-wall boundary layers[51] and the effect of removing the boundary layers on the liners.[51] Symmetry conditions were applied at the y-wise and z-wise symmetry planes and an adiabatic no-slip condition at the solid walls. At the outflow boundary ($x = x_o$) the pressure signal is imposed, described as the sum of 12 time harmonics obtained from the measurements[10]

$$\bar{p}(t, x_o, y, z) = p_o(t) = {}^0p_o + \sum_{m=1}^{12} \left[\left| {}^m\hat{p}_o \right| \cos\left(2\pi m f t + {}^m\varphi_o\right) \right] \qquad \forall y, z \quad (26)$$

where ${}^0p_o$ is the time-mean outflow pressure, $|{}^m\hat{p}_o|$ and ${}^m\varphi_o$ the amplitudes and phase angles of the Fourier coefficients, and m the harmonic number. The outflow boundary condition imposes the pressure [and its time derivative in the implicit phase of the scheme, which is easily computed[10] from Eq. (26)] and extrapolates all other variables.[44] To achieve high time steps, it is indispensible to apply boundary conditions both implicitly[44] and explicitly.

Unsteady computations were started from a converged steady-state flowfield, corresponding to the average backpressure between the two extreme positions of the rod.[10] The computations converge to a periodic state after the simulation of two periods[10] (Figs. 4–6). An $[N_{PP}, CFL^*; M_{it}, r_{MF}] = [360, 20; -, -1.5]$ DTS time-integration scheme was used, which, based on the previous NACA-0012 oscillating airfoil study, seems adequate. Computations for three rod-rotation frequencies ($f = 20$, 80, 180 Hz) show quite satisfactory agreement with measurements (Figs. 4–6), both for the time signals of unsteady pressures $\bar{p}(t) - \langle \bar{p} \rangle$ and for the x-wise distribution of

Table 2 Influence of time-integration DTS scheme parameters N_{PP} and r_{MF} on computing time requirements for the CT5 test case[50] (NACA-0012 airfoil oscillating in pitch around $\frac{1}{4}\chi$, $M_\infty = 0.755$, $Re_\chi = 5.5 \times 10^6$, $Sr_\chi = 0.0259$; grid B)

N_{PP}	r_{MF}	CFL^*	M_{it}[a]	CFL_{max}	CPU, s[b]
90	−1.5	10	13–22	17.4×10^5	111
180	−1.5	10	11–23	8.7×10^5	199
360	−1.5	10	9–19	4.4×10^5	356
720	−1.5	10	9–16	2.2×10^5	663
1440	−1.5	10	8–16	1.4×10^5	1268
360	−1.0	10	7–9	4.4×10^5	233
360	−1.5	10	9–19	4.4×10^5	356
360	−2.0	10	12–52	4.4×10^5	548
360	−2.3	10	18–92	4.4×10^5	769

[a]Number of subiterations required to reduce the error in the time increment r_{MF} to the required value.
[b]CPU required for the simulation of one oscillation period on a NEC-SX5 computer using a 2-Gflops code.

Table 3 Computational grids used for the discretization of $\frac{1}{4}$ of the Ott et al.[51] transonic channel

Grid	$N_i\,(N_x)^{a,b}$	$N_j\,(N_y)^{a,b}$	$N_k\,(N_z)^{a,b}$	Points	y_w^{+c}	z_w^{+c}	$r_j{}^d$	$r_k{}^d$	L_x, m[e]	L_y, m[e]	L_z, m[e]
A	121	57	49	0.34×10^6	∼0.5	∼0.5	1.182	1.194	0.264	0.04	0.02
B	201	57	49	0.56×10^6	∼0.5	∼0.5	1.182	1.194	0.264	0.04	0.02
C	201	111	91	2.03×10^6	∼0.5	∼0.5	1.081	1.09	0.264	0.04	0.02

[a]i, j, k = grid directions.
[b]N_i, N_j, N_k = number of points.
[c]y_w^+, z_w^+ = nondimensional distance of the first grid node away from the wall.
[d]r_j, r_k = geometric progression ratio.
[e]L_x, L_y, L_z = length.

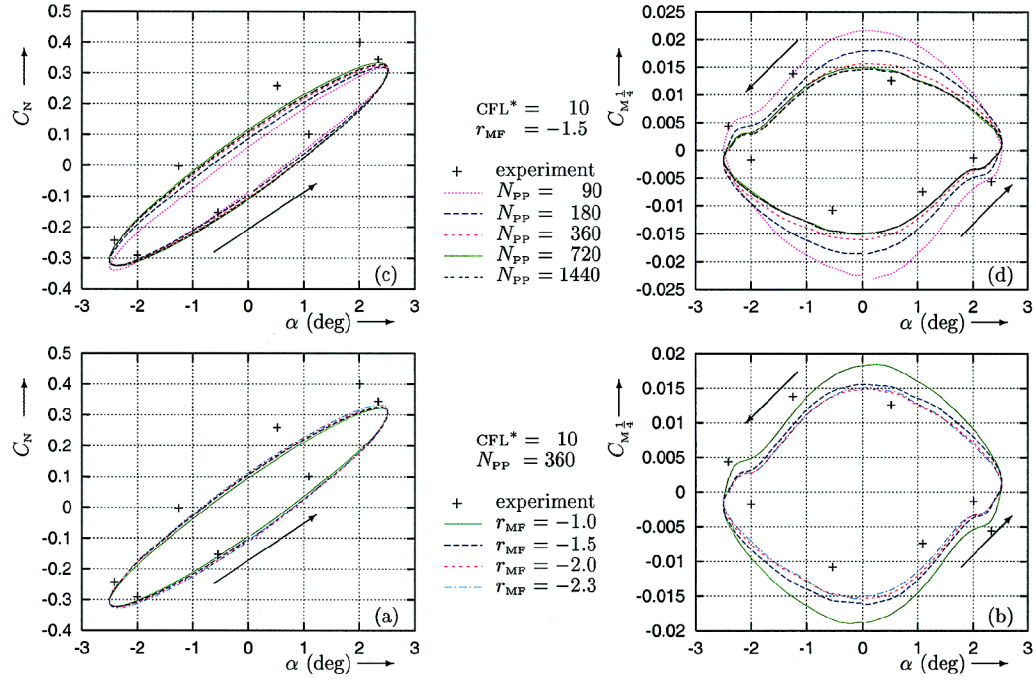

Fig. 3 Comparison of measured[50] normal force coefficient C_N and pitching-moment coefficient $C_{M1/4}$ as a function of instantaneous angle of attack and computed results, using an RSM closure[35] and different numbers of instants per period (N_{PP} = 90, 180, 360, 720, 1440) with a fixed reduction $r_{MF} = -1.5$ and different reduction values ($r_{MF} = -1, -1.5, -2, -2.3$) with a fixed $N_{PP} = 360$ (NACA-0012 airfoil oscillating in pitch around $\frac{1}{4}\chi$, $M_\infty = 0.755$, $Re_\chi = 5.5 \times 10^6$, $Sr_\chi = 0.0259$; grid B).

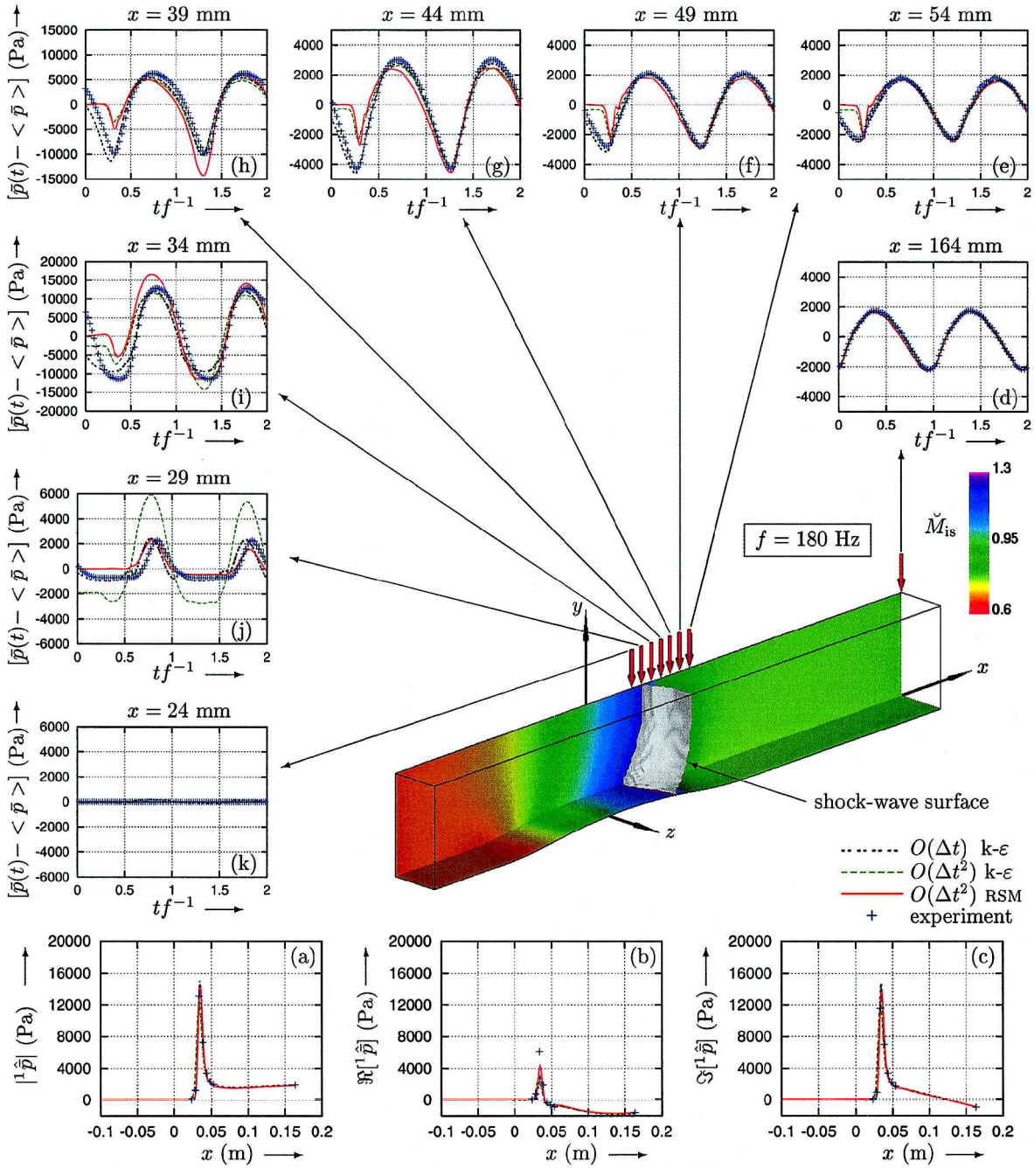

Fig. 4 Comparison of computed [using the Launder–Sharma[62] k–ε model, both with an $\mathcal{O}(\Delta t)$ AF-ADI non-DTS scheme[10] and with an $\mathcal{O}(\Delta t^2)$ [N_{PP}, CFL^*; M_{it}, r_{MF}] = [360, 20; −, −1.5] DTS scheme and using the wall-normal-free version[38] of the Launder–Shima[52] RSM with the same $\mathcal{O}(\Delta t^2)$ DTS scheme] and measured[51] unsteady pressures (d–k) at various axial locations at the y-wise symmetry plane on the side wall of the Ott et al.[51] nozzle and x-wise distributions of the pressure harmonic ${}^1\hat{\bar{p}}$ (a–c) for a frequency f = 180 Hz [$\mathcal{O}(\Delta t)$ k–ε, grid A; $\mathcal{O}(\Delta t^2)$ k–ε, grid B; RSM, grid C].

the first-pressure harmonic ${}^1\hat{\bar{p}}$, where

$$\langle \bar{p} \rangle \equiv {}^0\bar{p} = f \int_{t_0}^{t_0 + f^{-1}} \bar{p}(t)\, \mathrm{d}t$$

$${}^m\hat{\bar{p}} = \Re({}^m\hat{\bar{p}}) + i\Im({}^m\hat{\bar{p}}) = 2f \int_{t_0}^{t_0 + f^{-1}} \bar{p}(t) e^{-i2\pi m f t}\, \mathrm{d}t \qquad (27)$$

For the higher frequency (f = 180 Hz; Fig. 4) the previously published non-DTS $\mathcal{O}(\Delta t)$ k–ε computations[10] are included as well. The agreement between the three computations and measured unsteady pressures (Figs. 4d–4k) is excellent, with the exception of the DTS $\mathcal{O}(\Delta t^2)$ k–ε computation at x = 29 mm (Fig. 4j), which slightly overestimates the unsteady pressure amplitude. However, the unsteady pressure plot scale is different on each plot (Figs. 4d–4k), so that the discrepancy is in reality slight and is not visible on the ${}^1\hat{\bar{p}}$ x-wise distributions (Figs. 4a–4c). This difference between the non-DTS $\mathcal{O}(\Delta t)$ and the DTS $\mathcal{O}(\Delta t^2)$ k–ε computations is in reality caused by the use of different limiters for the MUSCL variables between the two computations, which introduces a slight difference in the position of the steady shock wave. For the intermediate (f = 80 Hz; Fig. 5) and for the lower (f = 20 Hz; Fig. 6) frequencies, the agreement between the DTS $\mathcal{O}(\Delta t^2)$ computations (k–ε and RSM) and the measurements is quite good, despite some small discrepancies in the shock-wave neighborhood between the two computations. These discrepancies are attributed to a slight difference in the steady shock-wave position predicted by each model, mainly because different grids were used for each model. Note in particular the differences in the k–ε

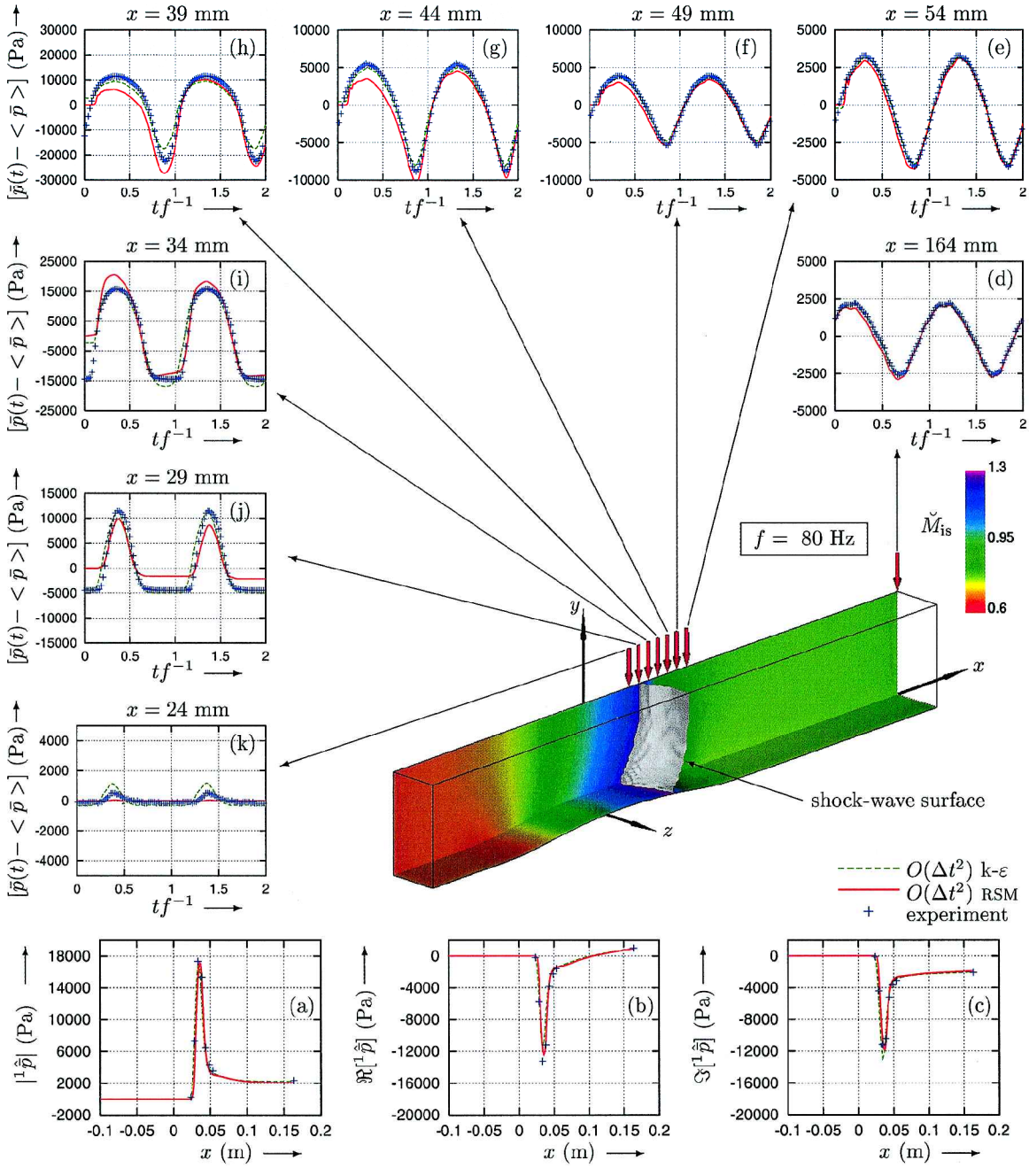

Fig. 5 Comparison of computed [using the Launder–Sharma[62] k–ε model and the wall-normal-free version[38] of the Launder–Shima[52] RSM with the $\mathcal{O}(\Delta t^2)$ [N_{PP}, CFL^*; M_{it}, r_{MF}] = [360, 20; −, −1.5] DTS scheme] and measured[51] unsteady pressures (d–k) at various axial locations at the y-wise symmetry plane on the side wall of the Ott et al.[51] nozzle and x-wise distributions of the pressure harmonic $^1\hat{\bar{p}}$ (a–c) for a frequency f = 80 Hz (k–ε, grid A; RSM, grid C).

computations using two different grids (Fig. 4), clearly indicating that the observed discrepancies are not significant in comparing turbulence models. This is also corroborated by considering the x-wise distributions of $^1\hat{\bar{p}}$ (Figs. 4–6), where differences are indeed slight.

Interesting conclusions can be drawn from a close examination of the computing time requirements between various computations (Table 4). As far as the computational time per grid point and per subiteration $\delta\text{CPU}_{m_{it}}$ of the two turbulence models is concerned, the RSM overhead compared to k–ε is ∼26% (because of the careful design of approximate Jacobians[42]). Furthermore, the number of subiterations required for the two models (grid A, $f = 180$ Hz; Table 4) to obtain a given increment-error reduction r_{MF} is approximately the same. This leads to the conclusion that the overall computing time overhead of the RSM computations compared to k–ε computations is roughly 26%. Consideration of the DTS k–ε computations for the three different frequencies (grid A) shows that, for a given number of instants per period N_{PP} and a given increment-error reduction r_{MF}, M_{it} increases slowly with decreasing frequency (as f diminishes by a factor 9 between 180 and 20 Hz, and, for a constant $N_{PP} = 360$, the physical time step Δt increases by the same factor; the number of subiterations M_{it} only doubles). Quite high CFL_{max} are obtained (Table 4), especially for the RSM computations on the 2.03×10^6 points grid C (up to $CFL_{max} = 3.42 \times 10^6$ for the lowest frequency $f = 20$ Hz), demonstrating the robustness of the method. Note again that the number of subiterations M_{it} increases much slower than CFL_{max} (Table 4). Finally, comparison with the preceding non-DTS AF-ADI computations[10] indicates a factor 4 gain in CPU time for the highest frequency $f = 180$ Hz when using the DTS scheme. (This gain would be of ∼30 for the lowest frequency $f = 20$ Hz because for the non-DTS method N_{PP} is inversely proportional to frequency.)

Table 4 Computing time requirements for the computation of three periods of rod rotation of $\frac{1}{4}$ of the Ott et al.[51] transonic channel

Grid[a]	$N_i \times N_j \times N_k$ [b,c]	f, Hz[d]	Closure[e]	Scheme[f]	$CFL_{\max}$ [g]	M_{it} [h]	$\delta\text{CPU}_{m_{it}}$, μs[i]	CPU, h[j]
A	0.34×10^6	180	k–ε	[30744, ∞; 1, −] (ADI[10])	250	1	∼5.8	50.6
A	0.34×10^6	180	k–ε	[15408, ∞; 1, −] (ADI[10])	500	1	∼5.8	25.3
A	0.34×10^6	180	k–ε	[720, 20; −, −1.5] (DTS)	0.08×10^6	9–13	∼5.8	14.9
A	0.34×10^6	180	k–ε	[360, 20; −, −1.5] (DTS)	0.16×10^6	10–13	∼5.8	7.5
A	0.34×10^6	180	RSM	[360, 20; −, −1.5] (DTS)	0.16×10^6	10–13	∼7.3	9.2
A	0.34×10^6	80	k–ε	[360, 20; −, −1.5] (DTS)	0.36×10^6	12–18	∼5.8	9.4
A	0.34×10^6	20	k–ε	[360, 20; −, −1.5] (DTS)	1.44×10^6	18–23	∼5.8	13.2
B	0.56×10^6	180	k–ε	[360, 20; −, −1.5] (DTS)	0.22×10^6	11–14	∼5.8	12.7
C	2.03×10^6	180	RSM	[360, 20; −, −1.5] (DTS)	0.38×10^6	15–18	∼7.3	71.1
C	2.03×10^6	80	RSM	[360, 20; −, −1.5] (DTS)	0.86×10^6	18–22	∼7.3	83.4
C	2.03×10^6	20	RSM	[360, 20; −, −1.5] (DTS)	3.42×10^6	23–28	∼7.3	111.6

[a] Grid = grid used (Table 3).
[b] i, j, k = grid directions.
[c] N_i, N_j, N_k = number of points.
[d] f = frequency of rotation of the rod.
[e] Closure = turbulence model used (k–ε[62] or RSM[38]).
[f] Scheme = time-integration parameters ([N_{PP}, CFL^*; M_{it}, r_{MF}]).
[g] $CFL_{\max}$ = maximum value of CFL number.
[h] M_{it} = required number of subiterations.
[i] $\delta\text{CPU}_{m_{it}}$ = CPU time per grid point required for one subiteration with a 2-Gflops sustained performance code.
[j] CPU = CPU-time (h) required for the computation of three periods with a 2-Gflops sustained performance code (previous ADI computations[10] CPU time requirements were scaled to the current code performance).

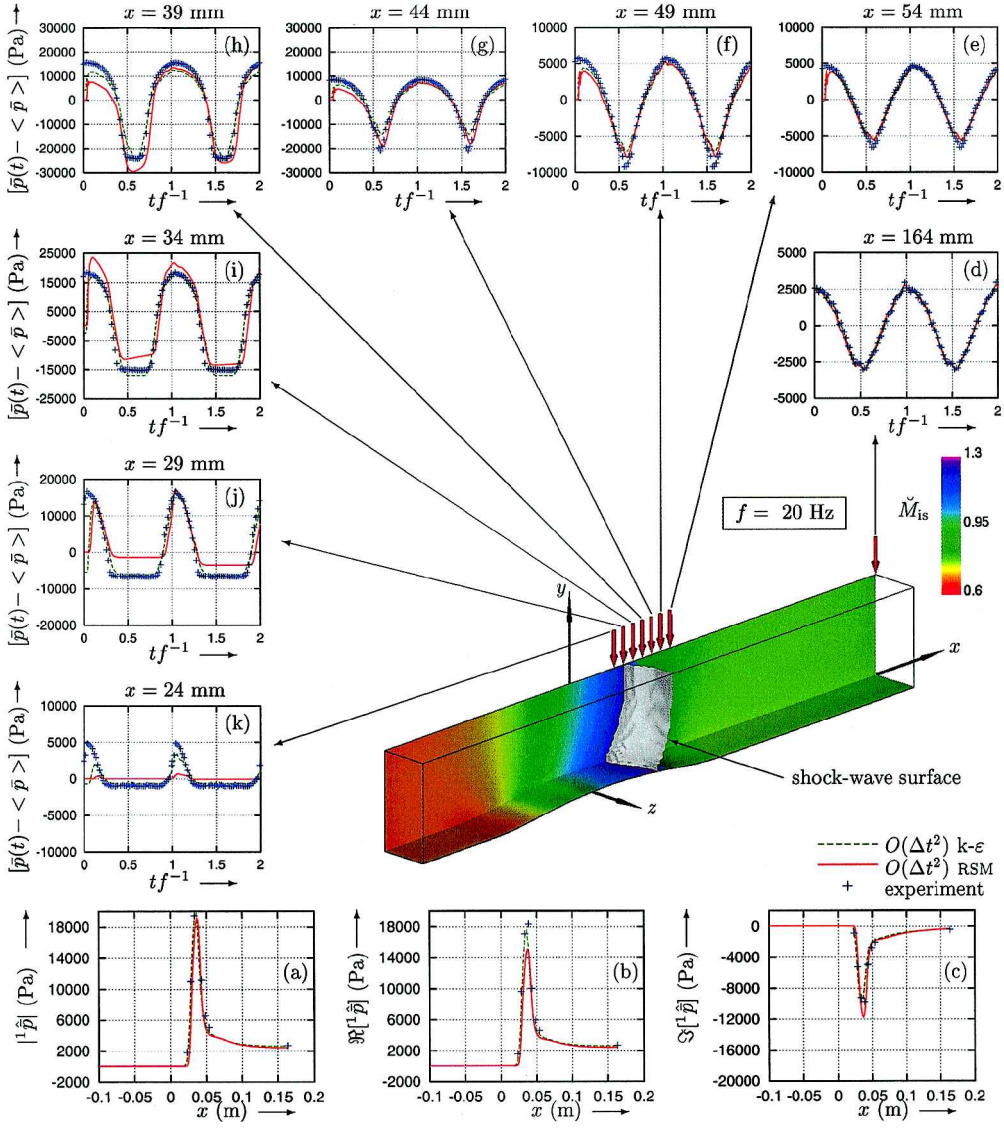

Fig. 6 Comparison of computed [using the Launder–Sharma[62] k–ε model and the wall-normal-free version[38] of the Launder–Shima[52] RSM, with the $\mathcal{O}(\Delta t^2)$ [N_{PP}, CFL^*; M_{it}, r_{MF}] = [360, 20; −, −1.5] DTS scheme] and measured[51] unsteady pressures (d–k) at various axial locations at the y-wise symmetry plane on the side wall of the Ott et al.[51] nozzle and x-wise distributions of the pressure-harmonic ${}^1\hat{\bar{p}}$ (a–c) for a frequency f = 20 Hz (k–ε, grid A; RSM, grid C).

Conclusions

In the present work a computational methodology for the numerical integration of the unsteady Favre–Reynolds-averaged Navier–Stokes equations with near-wall RSM closure was presented and analyzed, yielding the following conclusions:

1) A careful $\mathcal{O}(\Delta x^3)$ upwind-biased implicit implementation of the RSM closure, with explicit application of appropriate realizability constraints, yields a particularly robust method allowing the routine computation of complex unsteady flows. Computational efficiency is achieved by using approximate Jacobians, in the implicit phase, which uncouple the mean-flow (MF) equations from the RSM equations (while retaining the feedback of MF increments on the RSM equations), so that the implicit phase of the RSM equations corresponds to an implicit scalar approximation. In this way the overall computational cost of the RSM seven-equation closure computations is only ~26% higher than the cost of two-equation closures (compared to a factor 3–4 overhead when not using approximate Jacobians).

2) The unsteady computations are run using an $\mathcal{O}(\Delta t^2)$ implicit DTS scheme, where the number of subiterations is dynamically chosen to obtain a given level of convergence (r_{MF}) of the increments. The method achieves quite high physical time steps ($CFL_{\max} \sim 10^6 - 10^7$), using the RSM closure in three-dimensional transonic flows, with a reasonable number of required subiterations ($M_{\mathrm{it}} \sim 10 - 20$). Subiterations are based on an ADI-AF method with pseudo-time steps $CFL^* = 10 - 20$.

3) Comparison of two-dimensional computations for the AGARD-CT5 test case of a NACA-0012 airfoil oscillating in pitch shows satisfactory agreement with measurements (and highlights the experimental setup bias of unexpected upper/lower side asymmetry). Systematic tests of computational parameters indicate that a logarithmic reduction of the increment convergence $r_{\mathrm{MF}} = -1.5$, associated with $N_{\mathrm{PP}} = 360$ instants per period, is a satisfactory choice.

4) Comparison of three-dimensional computations with measurements for shock-wave oscillation in a transonic nozzle show quite satisfactory agreement for the entire range of experimentally studied frequencies (0–180 Hz) and demonstrate the robustness of the RSM methodology. They also substantiate the conclusion that the overhead of the RSM computations compared to two-equation closures is only ~26%. Small discrepancies are observed, in the shock-wave neighborhood, between various computations. These discrepancies are attributed to a slight difference in the steady shock-wave position predicted by each model, mainly because different grids were used for each model, and are not significant in comparing turbulence models.

It is believed that the present work contributes in demonstrating the feasibility of efficient and robust unsteady solvers with near-wall wall-normal-free RSMs, and it is hoped that the method developed will allow testing and assessment of RSM closures in complex unsteady flows.

Acknowledgments

The computations presented in this work were run at the Institut pour le Développement des Ressources en Informatique Scientifique, where computer resources were made available by the Comité Scientifique. The authors thank A. Bölcs and P. Ott of the Ecole Polytechnique Fédérale de Lausanne for providing the experimental data. The authors are listed alphabetically.

References

[1]Rai, M. M., "3-D Navier–Stokes Simulations of Turbine Rotor/Stator Interaction; Part I—Methodology," *Journal of Propulsion and Power*, Vol. 5, No. 3, 1989, pp. 305–311.

[2]Hah, C., Puterbaugh, S. L., and Copenhaver, W. W., "Unsteady Aerodynamic Flow Phenomena in a Transonic Compressor Stage," *Journal of Propulsion and Power*, Vol. 13, No. 3, 1997, pp. 329–333; also AIAA Paper 93-1868, June 1993.

[3]Sayma, A. I., Vahdati, M., Sbardella, L., and Imregun, M., "Modeling of Three-Dimensional Viscous Compressible Turbomachinery Flows Using Unstructured Hybrid Grids," *AIAA Journal*, Vol. 38, No. 6, 2000, pp. 945–954.

[4]Volmar, T. W., Brouillet, B., Gallus, H. E., and Benetschik, H., "Time-Accurate Three-Dimensional Navier–Stokes Analysis of $1\frac{1}{2}$ stage Axial-Flow Turbine," *Journal of Propulsion and Power*, Vol. 16, No. 2, 2000, pp. 327–335.

[5]Yao, J., Davis, R. L., Alonso, J. J., and Jameson, A., "Massively Parallel Simulation of the Unsteady Flow in an Axial Turbine Stage," *Journal of Propulsion and Power*, Vol. 18, No. 2, 2002, pp. 465–471.

[6]Obahashi, S., Guruswamy, G. P., and Goorjian, P. M., "Streamwise Upwind Algorithm for Computing Unsteady Transonic Flows past Oscillating Wings," *AIAA Journal*, Vol. 29, No. 10, 1991, pp. 1668–1677.

[7]Lee-Rausch, E. M., and Batina, J. T., "Wing Flutter Computations Using an Aerodynamic Model Based on the Navier–Stokes Equations," *Journal of Aircraft*, Vol. 33, No. 6, 1996, pp. 1139–1147.

[8]Gordnier, R. E., and Melville, R. B., "Transonic Flutter Simulations Using an Implicit Aeroelastic Solver," *Journal of Aircraft*, Vol. 37, No. 5, 2000, pp. 872–879.

[9]Weber, S., and Platzer, M. F., "A Navier–Stokes Analysis of the Stall Flutter Characteristics of the Buffum Cascade," *Journal of Turbomachinery*, Vol. 122, Oct. 2000, pp. 769–776.

[10]Gerolymos, G. A., Vallet, I., Bölcs, A., and Ott, P., "Computation of Unsteady Three-Dimensional Transonic Nozzle Flow Using k–ε Turbulence Closure," *AIAA Journal*, Vol. 34, No. 7, 1996, pp. 1321–1330.

[11]Hah, C., Rabe, D. C., Sullivan, T. J., and Wadia, A. R., "Effects of Inlet Distortion on the Flow Field in a Transonic Compressor Rotor," *Journal of Turbomachinery*, Vol. 120, April 1998, pp. 233–246.

[12]Ekaterinaris, J. A., "Numerical Investigations of Dynamic Stall Active Control for Incompressible and Compressible Flows," *Journal of Aircraft*, Vol. 39, No. 1, 2002, pp. 71–78.

[13]Liou, M. S., and Coakley, T. J., "Numerical Simulations of Unsteady Transonic Flow in Diffusers," *AIAA Journal*, Vol. 22, No. 8, 1984, pp. 1139–1145.

[14]Hsieh, T., Bogar, T. J., and Coakley, T. J., "Numerical Simulation and Comparison with Experiment for Self-Excited Oscillations in a Diffuser Flow," *AIAA Journal*, Vol. 25, No. 7, 1987, pp. 936–943.

[15]Rizzetta, D. P., "Numerical Simulation of Supersonic Flow over a 3-D Cavity," *AIAA Journal*, Vol. 26, No. 7, 1988, pp. 799–807.

[16]Yamamoto, K., and Tanida, Y., "Self-Excited Oscillation of Transonic Flow Around an Airfoil in 2-D Channels," *Journal of Turbomachinery*, Vol. 112, Oct. 1990, pp. 723–731.

[17]He, L., "Computational Study of Rotating Stall Inception in Axial Compressors," *Journal of Propulsion and Power*, Vol. 13, No. 1, 1997, pp. 31–38.

[18]Hartwich, P. M., Dobbs, S. K., Arslan, A. E., and Kim, S. C., "Navier–Stokes Computations of Limit-Cycle Oscillations for a B-1-Like Configuration," *Journal of Aircraft*, Vol. 38, No. 2, 2001, pp. 239–247.

[19]Weber, S., Jones, K. D., Ekaterinaris, J. A., and Platzer, M., "Transonic Flutter Computations for the NLR 7301 Supercritical Airfoil," *Aerospace Science and Technology*, Vol. 5, 2001, pp. 293–304.

[20]Grüber, B., and Carstens, V., "The Impact of Viscous Effects on the Aerodynamic Damping of Vibrating Transonic Compressor Blades—A Numerical Study," *Journal of Turbomachinery*, Vol. 123, 2001, pp. 409–417.

[21]Tardu, S. F., and Binder, G., "Wall Shear Stress Modulation in Unsteady Turbulent Channel Flow with High Imposed Frequencies," *Physics of Fluids A*, Vol. 5, No. 8, 1993, pp. 2028–2037.

[22]Fan, S., Lakshminarayana, B., and Barnett, M., "Low-Reynolds-Number k–ε Model for Unsteady Turbulent Boundary-Layer Flows," *AIAA Journal*, Vol. 31, No. 10, 1993, pp. 1777–1784.

[23]Hankey, W. L., and Calarese, W., "Reynolds Stresses for Unsteady Turbulent Flows," *AIAA Journal*, Vol. 21, No. 8, 1983, pp. 1210, 1211.

[24]Rizzetta, D. P., and Visbal, M. R., "Comparative Numerical Study of Two Turbulence Models for Airfoil Static and Dynamic Stall," *AIAA Journal*, Vol. 31, No. 4, 1993, pp. 784–786.

[25]Ekaterinaris, J. A., and Menter, F. R., "Computation of Oscillating Airfoil Flows with One- and Two-Equation Turbulence Models," *AIAA Journal*, Vol. 32, No. 12, 1994, pp. 2359–2365.

[26]Ji, S., and Liu, F., "Flutter Computation of Turbomachinery Cascades Using a Parallel Unsteady Navier–Stokes Code," *AIAA Journal*, Vol. 37, No. 3, 1999, pp. 320–327.

[27]Choi, S. W., Chang, K. S., and Ok, H., "Parametric Study of Transient Spoiler Aerodynamics with 2-Equation Turbulence Models," *Journal of Aircraft*, Vol. 38, No. 5, 2001, pp. 888–894.

[28]Hanjalić, K., "Advanced Turbulence Closure Models: A View of Current Status and Future Prospects," *International Journal of Heat Fluid Flow*, Vol. 15, No. 3, 1994, pp. 178–203.

[29]Rodi, W., "A New Algebraic Relation for Calculating the Reynolds Stresses," *Zeitschrift für Angewandte Mathematik und Mechanik*, Vol. 56, 1976, pp. T219–T221.

[30]Gatski, T. B., and Speziale, C. G., "On Explicit Algebraic Stress Models for Complex Turbulent Flows," *Journal of Fluid Mechanics*, Vol. 254, 1993, pp. 59–78.

[31]Sotiropoulos, F., and Patel, V. C., "Application of Reynolds-Stress Transport Models to Stern and Wake Flows," *Journal of Ship Research*, Vol. 39, No. 4, 1995, pp. 263–283.

[32]Gerolymos, G. A., and Vallet, I., "Near-Wall Reynolds-Stress Three-Dimensional Transonic Flow Computation," *AIAA Journal*, Vol. 35, No. 2, 1997, pp. 228–236.

[33]Chenault, C. F., Beran, P. S., and Bowersox, R. D. W., "Numerical Investigation of Supersonic Injection Using a Reynolds-Stress Turbulence Model," *AIAA Journal*, Vol. 37, No. 10, 1999, pp. 1257–1269.

[34]Batten, P., Craft, T. J., Leschziner, M. A., and Loyau, H., "Reynolds-Stress-Transport Modeling for Compressible Aerodynamics Applications," *AIAA Journal*, Vol. 37, No. 7, 1999, pp. 785–797.

[35]Gerolymos, G. A., and Vallet, I., "Wall-Normal-Free Reynolds-Stress Closure for Three-Dimensional Compressible Separated Flows," *AIAA Journal*, Vol. 39, No. 10, 2001, pp. 1833–1842.

[36]Gerolymos, G. A., Neubauer, J., Sharma, V. C., and Vallet, I., "Improved Prediction of Turbomachinery Flows Using Near-Wall Reynolds-Stress Model," *Journal of Turbomachinery*, Vol. 124, Jan. 2002, pp. 86–99.

[37]Pettersson, B. A., Andersson, H. I., and Brunvoll, A. S., "Modeling near-Wall Effects in Axially Rotating Pipe Flow by Elliptic Relaxation," *AIAA Journal*, Vol. 36, No. 7, 1998, pp. 1164–1170.

[38]Gerolymos, G. A., and Vallet, I., "Contribution to Single-Point-Closure Reynolds-Stress Modelling in Inhomogeneous Flow," American Society of Mechanical Engineers, Paper FEDSM2003-45346, July 2003.

[39]Jakirlić, S., and Hanjalić, K., "A New Approach to Modelling near-Wall Turbulence Energy and Stress Dissipation," *Journal of Fluid Mechanics*, Vol. 459, 2002, pp. 139–166.

[40]Pantano, C., and Sarkar, S., "A Study of Compressibility Effects in the High-Speed Turbulent Shear Layer Using Direct Simulation," *Journal of Fluid Mechanics*, Vol. 451, 2002, pp. 329–371.

[41]Wilcox, D. C., "Multiscale Model for Turbulent Flows," *AIAA Journal*, Vol. 26, No. 11, 1988, pp. 1311–1320.

[42]Chassaing, J. C., Gerolymos, G. A., and Vallet, I., "Efficient and Robust Reynolds-Stress Model Computation of Three-Dimensional Compressible Flows," *AIAA Journal*, Vol. 41, No. 5, 2003, pp. 763–773.

[43]Morrison, J. H., "A Compressible Navier–Stokes Solver with 2-Equation and Reynolds-Stress Turbulence Closure Models," NASA CR 4440, May 1992.

[44]Vallet, I., "Aérodynamique Numérique 3-D Instationnaire avec Fermeture Bas-Reynolds au Second Ordre," Ph.D. Dissertation, Université Pierre-et-Marie-Curie, Paris, Dec. 1995.

[45]Batten, P., Leschziner, M. A., and Goldberg, U. C., "Average-State Jacobians and Implicit Methods for Compressible Viscous and Turbulent Flows," *Journal of Computational Physics*, Vol. 137, 1997, pp. 38–78.

[46]Rogers, S. E., Kwak, D., and Kris, C., "Steady and Unsteady Solutions of the Incompressible Navier–Stokes Equations," *AIAA Journal*, Vol. 29, No. 4, 1991, pp. 603–610.

[47]Jameson, A., "Time-Dependent Calculations Using Multigrid, with Applications to Unsteady Flows past Airfoils and Wings," AIAA Paper 91-1596, June 1991.

[48]Rumsey, C. L., Sanetrik, M. D., Bierdon, R. T., Melson, N. D., and Parlette, E. B., "Efficiency and Accuracy of Time-Accurate Turbulent Navier–Stokes Computations," *Computers and Fluids*, Vol. 25, No. 2, 1996, pp. 217–236.

[49]Dubuc, L., Cantariti, F., Woodgate, M., Gribben, B., Badcock, K. J., and Richards, B. E., "Solution of the Unsteady Euler Equations Using an Implicit Dual-Time Method," *AIAA Journal*, Vol. 36, No. 8, 1998, pp. 1417–1424.

[50]Landon, R. H., "NACA_0012 Oscillatory and Transient Pictching," *Compendium of Unsteady Aerodynamic Measurements*, R-702, AGARD, 1982, pp. 3·1–3·25.

[51]Ott, P., Bölcs, A., and Fransson, T. H., "Experimental and Numerical Study of the Time-Dependent Pressure Response of a Shock-Wave Oscillating in a Nozzle," *Journal of Turbomachinery*, Vol. 117, Jan. 1995, pp. 106–114.

[52]Launder, B. E., and Shima, N., "2-Moment Closure for the near-Wall Sublayer: Development and Application," *AIAA Journal*, Vol. 27, No. 10, 1989, pp. 1319–1325.

[53]Thomas, P. D., and Lombard, C. K., "Geometric Conservation Law and its Application to Flow Computations on Moving Grids," *AIAA Journal*, Vol. 17, No. 10, 1979, pp. 1030–1037.

[54]Slater, J. W., Liou, M. S., and Hindman, R. G., "Approach for Dynamic Grids," *AIAA Journal*, Vol. 33, No. 1, 1995, pp. 63–68.

[55]Hixon, R., "Numerically Consistent Strong Conservation Grid Motion for Finite-Difference Schemes," *AIAA Journal*, Vol. 38, No. 9, 2000, pp. 1586–1593.

[56]Anderson, W. K., Thomas, J. L., and Rumsey, C. L., "Extension and Application of Flux-Vector-Splitting to Calculations on Dynamic Meshes," *AIAA Journal*, Vol. 27, No. 6, 1989, pp. 673, 674; also AIAA Paper 87-1152, June 1987.

[57]Anderson, W. K., Thomas, J. L., and Van Leer, B., "Comparison of Finite-Volume Flux-Vector-Splittings for the Euler Equations," *AIAA Journal*, Vol. 24, No. 9, 1986, pp. 1453–1460.

[58]Thomas, J. L., Taylor-Krist, S., and Anderson, W. K., "Navier–Stokes Computations of Vortical Flows over Low-Aspect-Ratio Wings," *AIAA Journal*, Vol. 28, No. 2, 1990, pp. 205–212.

[59]Chassaing, J. C., "Aérodynamique 3-D et Aéroélasticité Nonlinéaire et Linéarisée en Temps," Ph.D. Dissertation, Université Pierre-et-Marie-Curie, Paris, Jan. 2002.

[60]Schumann, U., "Realizability of Reynolds-Stress Turbulence Models," *Physics of Fluids*, Vol. 20, No. 5, 1977, pp. 721–725.

[61]Gerolymos, G. A., and Tsanga, G., "Biharmonic 3-D Grid Generation for Axial Turbomachinery with Tip-Clearance," *Journal of Propulsion and Power*, Vol. 15, No. 3, 1999, pp. 476–479.

[62]Launder, B. E., and Sharma, B. I., "Application of the Energy Dissipation Model of Turbulence to the Calculation of Flows near a Spinning Disk," *Letters in Heat and Mass Transfer*, Vol. 1, 1974, pp. 131–138.

W. J. Devenport
Associate Editor

Color reproductions courtesy of Université Pierre-et-Marie-Curie.